JGR Solid Earth

RESEARCH ARTICLE
10.1029/2021JB022488

A Compound Faulting Model for the 1975 Kalapana, Hawaii, Earthquake, Landslide, and Tsunami

Yoshiki Yamazaki[1], Thorne Lay[2], and Kwok Fai Cheung[1]

[1]Department of Ocean and Resources Engineering, University of Hawaii at Manoa, Honolulu, HI, USA, [2]Department of Earth and Planetary Sciences, University of California, Santa Cruz, CA, USA

Key Points:

- Compound faulting on décollement and near-surface crustal faults accounts for tsunami runup and tide gauge observations of the 1975 event
- Landslide block faulting extends from surface outcrops along the Hilina Fault System to 1–3 km deep shallowly dipping offshore faults
- Hilina block slide causes large near-field coastal runup, while décollement slip dominates longer-period far-field tsunami excitation

Supporting Information:

Supporting Information may be found in the online version of this article.

Correspondence to:

K. F. Cheung,
cheung@hawaii.edu

Citation:

Yamazaki, Y., Lay, T., & Cheung, K. F. (2021). A compound faulting model for the 1975 Kalapana, Hawaii, earthquake, landslide, and tsunami. *Journal of Geophysical Research: Solid Earth*, *126*, e2021JB022488. https://doi.org/10.1029/2021JB022488

Received 26 MAY 2021
Accepted 16 OCT 2021

Author Contributions:

Conceptualization: Yoshiki Yamazaki, Thorne Lay, Kwok Fai Cheung
Data curation: Yoshiki Yamazaki
Formal analysis: Yoshiki Yamazaki
Funding acquisition: Yoshiki Yamazaki
Investigation: Yoshiki Yamazaki, Thorne Lay, Kwok Fai Cheung
Methodology: Yoshiki Yamazaki, Thorne Lay, Kwok Fai Cheung
Project Administration: Yoshiki Yamazaki
Software: Yoshiki Yamazaki
Validation: Yoshiki Yamazaki
Visualization: Yoshiki Yamazaki
Writing – original draft: Thorne Lay, Kwok Fai Cheung
Writing – review & editing: Yoshiki Yamazaki, Thorne Lay, Kwok Fai Cheung

Abstract The Kalapana, Hawaii, M_W 7.7 earthquake on November 29, 1975 generated a local tsunami with at least 14.3 m runup on the southeast shore of Hawaii Island adjacent to Kilauea Volcano. This was the largest locally generated tsunami since the great 1868 Ka'u earthquake located along-shore to the southwest. Well-recorded tide gauge and runup observations provide a key benchmark for studies of statewide tsunami hazards from actively deforming southeast Hawaii Island. However, the source process of the earthquake remains controversial, with coastal landsliding and/or offshore normal or thrust faulting mechanisms having been proposed to reconcile features of seismic, geodetic, and tsunami observations. We utilize these diverse observations for the 1975 Kalapana earthquake to deduce a compound faulting model that accounts for the overall tsunamigenesis, involving both landslide block faulting along the shore and slip on the island basal décollement. Thrust slip of 4.5–8.0 m on the offshore décollement produces moderate near-field runup but controls the far-field tsunami. The slip distribution implies that residual strain energy was available for the May 4, 2018 M_W 7.2 thrust earthquake during the Kilauea-East Rift Zone eruption. Local faulting below land contributes to geodetic and seismic observations, but is non-tsunamigenic and not considered. Slip of 4–10 m on landslide-like faults, which extend from the Hilina Fault Zone scarp to offshore shallowly dipping faults reaching near the seafloor, triples the near-field tsunami runup. This compound model clarifies the roles of the faulting components in assessing tsunami hazards for the Hawaiian Islands.

Plain Language Summary On November 29, 1975, the Kalapana, Hawaii, earthquake with a seismic magnitude of 7.7 generated a tsunami reaching at least 14.3 m above sea level on the southeast shore of Hawaii Island adjacent to Kilauea Volcano. The largest locally generated event since the lesser documented, great 1868 Ka'u earthquake located to the southwest provides a key benchmark for studies of statewide tsunami hazards from volcanic activities on southeast Hawaii Island. We utilize seismic, tsunami, and land deformation observations to deduce the occurrence of both a massive block landslide from the Hilina Fault Zone and an offshore fracture along the island base during the earthquake. The inferred displacement of up to 8 m on the island base has moderate contributions to the local tsunami but controls the impact away from southeast Hawaii Island. The analysis suggests the1975 rupture left residual strain energy along the island base leading to the magnitude 7.2 earthquake during the Kilauea eruption on May 4, 2018. The up to 10 m displacement of the landslide block triples the local tsunami runup but with minor impacts away from Southeast Hawaii Island. This deduced earthquake mechanism clarifies the roles of landsliding and offshore fracturing in assessing tsunami hazards around the Hawaiian Islands.

1. Introduction

Mid-plate hot spot volcanic islands such as Hawaii involve basaltic edifices superimposed on depressed oceanic seafloor with basal décollement faults dipping landward at shallow angles (Figure 1a). Tsunamigenic thrust failure on the décollement or its splay faults can occur as topographic stresses and magma injection drive the island margins to spread (e.g., Borgia, 1994; Borgia & Treves, 1992; Chen et al., 2019; Day et al., 2005; Delaney et al., 1998; Dvorak et al., 1986; Gillard et al., 1996; Iverson, 1995; Moore & Krivoy, 1964; Nakamura, 1980; Owen et al., 1985; Swanson et al., 1976; Thurber & Gripp, 1988; Wyss & Koyanagi, 1992a; Wyss, 1988). Extensional faulting, landsliding, and submarine slumping from flank collapse also occur on island margins (e.g., Lipman et al., 1988; McMurtry et al., 2004; Moore et al., 1994), constituting additional sources of local tsunami hazard. Offshore structure on the island margin may involve benches with rotated

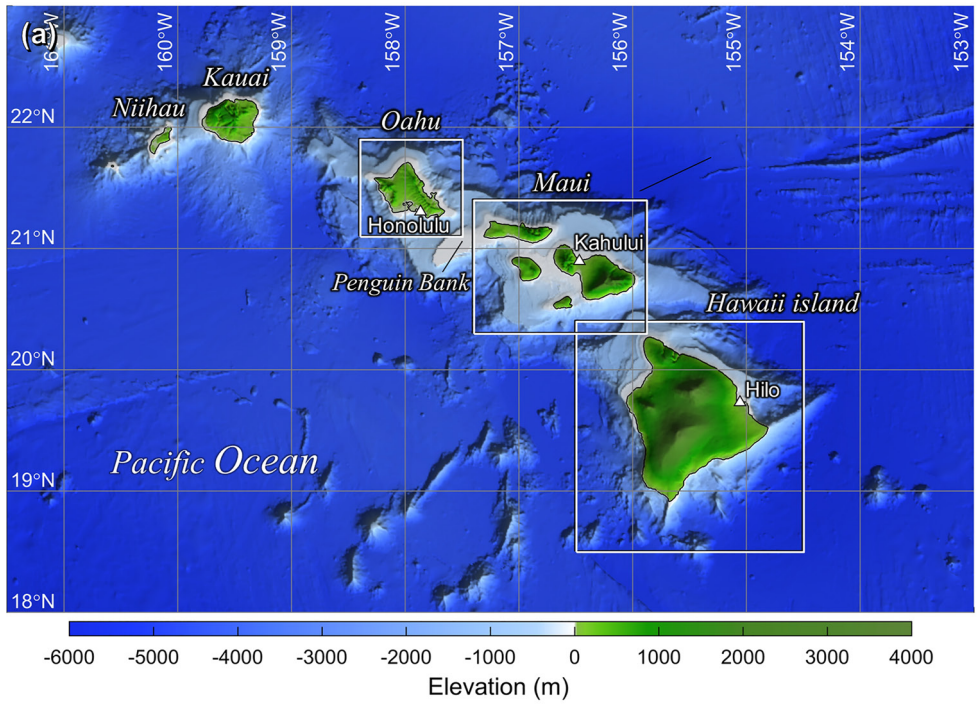

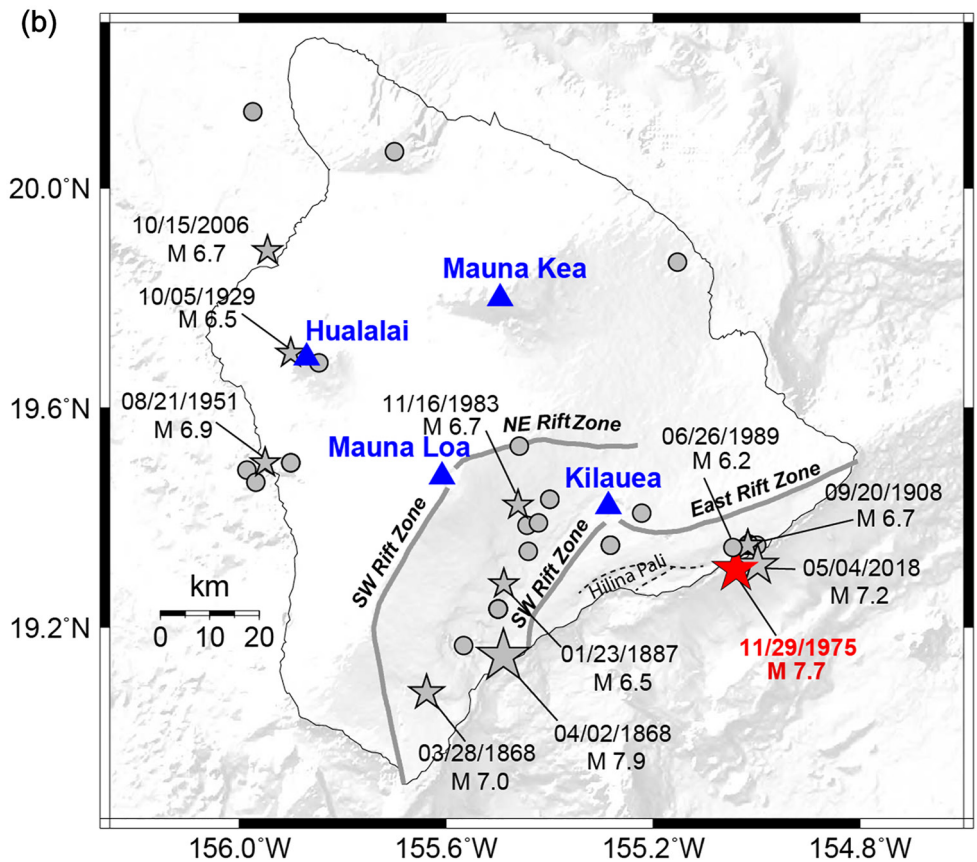

Figure 1. Relief, location, and seismicity maps. (a) Bathymetry and topography along the Hawaiian Islands with triangles locating the tide gauge stations used in this analysis. (b) Hawaii Island with locations of magnitude $M \geq 6.0$ earthquakes updated from Klein et al. (2001) for 1868–2018 (circles, or stars for events larger than M 6.5). Volcano summits are indicated by blue triangles, major rift zones on the flanks of Mauna Loa and Kilauea are labeled, along with the Halina Pali scarps. The November 29, 1975 M_W 7.7 earthquake hypocenter is indicated in red.

slump blocks and splay faults that do or do not connect to the décollement (e.g., Lipman et al., 1985; Moore et al., 1994; Morgan et al., 2000, 2003; Swanson et al., 1976). Loading rates for offshore faults around the Hawaiian Islands are usually difficult to determine, as seismicity is generally low, with large earthquakes being infrequent and portions of the décollement having a propensity for slow slip activity (e.g., Montgomery-Brown et al., 2009; Segall et al., 2006). Geodetic measurements provide constraints for on-land deformation of coastal margins and any relationship to volcanic intrusions (e.g., Delaney et al., 1998; Lipman et al., 1985; Owen & Bürgmann, 2006; Owen et al., 2000; Swanson et al., 1976), but the connection to offshore faulting is generally obscure.

The southeast shore of Hawaii Island, along the flanks of active volcanoes Kilauea and Mauna Loa, has historically experienced large, tsunamigenic earthquakes that impacted the Hawaiian Islands (Figure 1b). The April 2, 1868 Ka'u, Hawaii, earthquake of $M \sim 7.9$ is the largest known event (Hitchcock, 1912; Wood, 1914; Wyss, 1988), and it generated strong ground shaking along the entire southeast shore, with observed peak tsunami runup of 13.4 m above the mean sea level (MSL) at Keauhou Landing (Tilling et al., 1976). The décollement fault is the only tectonic structure extending both landward and offshore large enough to account for the strong shaking, but the décollement slip distribution and occurrence of any submarine landslide during the 1868 event are not known in detail. The November 29, 1975 Kalapana, Hawaii, earthquake had an epicenter about 50 km northeast from the estimated 1868 epicenter (Figure 1b) and produced an isoseismal pattern correspondingly shifted from that of the 1868 event, but with overlap along the flank of Kilauea (Wyss & Koyanagi, 1992a, 1992b). This event did not occur during an active eruption, and certainly involved near-surface crustal extensional faulting with vertical displacements up to 1.5 m on scarps along the 25-km long on-land Hilina Fault Zone (HFZ; Lipman et al., 1985). Large runup extended along the shoreline seaward of the HFZ with an observed peak of 14.3 m at Halape approximately 3 km west of Keauhou Landing (Tilling et al., 1976). Seaward ground motion occurred along the mobile south flank of Kilauea with minor horizontal and vertical deformation northeast of the epicenter and larger deformation along the shoreline seaward of the HFZ. The precise geometry of faulting and/or landslide motions associated with the observed ground deformation and the tsunami excitation has long been a topic of debate.

Ando (1979) used teleseismic *P* wave first-motions and *S* wave polarizations to infer that the 1975 earthquake involved a shallowly dipping (~10° southeastward) normal fault at about 10 km depth (Figures 2a and 2c). Radiation patterns for ~150 s period Love and Rayleigh waves were noted to both be pre-dominantly two-lobed (Figure 2e), but the Love wave radiation pattern was modeled as four-lobed in that study (Figure 2f). Furumoto & Kovach (1979) alternatively found that the *P* wave first-motions support a shallowly dipping (~4° northwestward) thrust event likely on the same décollement as that assumed to have ruptured in 1868 (Figure 2a). Eissler and Kanamori (1987) considered the predominantly two-lobed pattern for ~100 s period Love wave (G2) spectral amplitudes as evidence of near-surface coastal slumping (Figure 2b), and modeled the Kalapana source with a single-force model appropriate for a disaggregated landslide (Figures 2d and 2g). Wyss and Kovach (1988) contested the rationale for the slump model, arguing that shear displacement on a nearly horizontal fault plane could account for the two-lobed Love waves. Kawakatsu (1989) estimated a thrust plane dipping 19° toward the northwest from a long-period centroid-moment-tensor (CMT) inversion (Figure 2a), while Nettles and Ekström (2004) obtained a CMT thrust fault solution with a dip of 9° toward the northwest and a seismic moment, $M_0 = 3.8 \times 10^{20}$ Nm (M_W 7.7; Figure 2a). Neither of those point-source geometries accounts for the two-lobed Love wave pattern. Kawakatsu (1989) found that a double-couple source does fit the collective long-period signals better than a single-force source, but suggested that a composite of the two-force systems may be viable.

Ma et al. (1999) modeled tsunami observations at tide gauge stations in Hilo, Kahului, and Honolulu (Figure 1a), finding that a combination of a widespread propagating slump model and a 5° dipping décollement thrust fault model (with opposing 5° dipping bathymetry) gives reasonably good seismic waveform predictions. Lay et al. (2018) showed that thrust faulting with a dip of $\delta = 1$–4° (relative to the horizontal) to the northwest predicts predominantly two-lobed Love wave radiation patterns, largely accounting for the long-period observations of Ando (1979) and Eissler and Kanamori (1987), with an increased M_0 of $\sim 1 \times 10^{21}$ Nm (M_W 7.9; Figure 2h). The variation in the estimated seismic moment is due to excitation and radiation patterns for Rayleigh and Love waves being proportional to $M_0 \sin(2\delta)$ for shallow dip-slip dislocations with vanishing vertical strains at the free surface (e.g., Kanamori & Given, 1981). These shallowly dipping

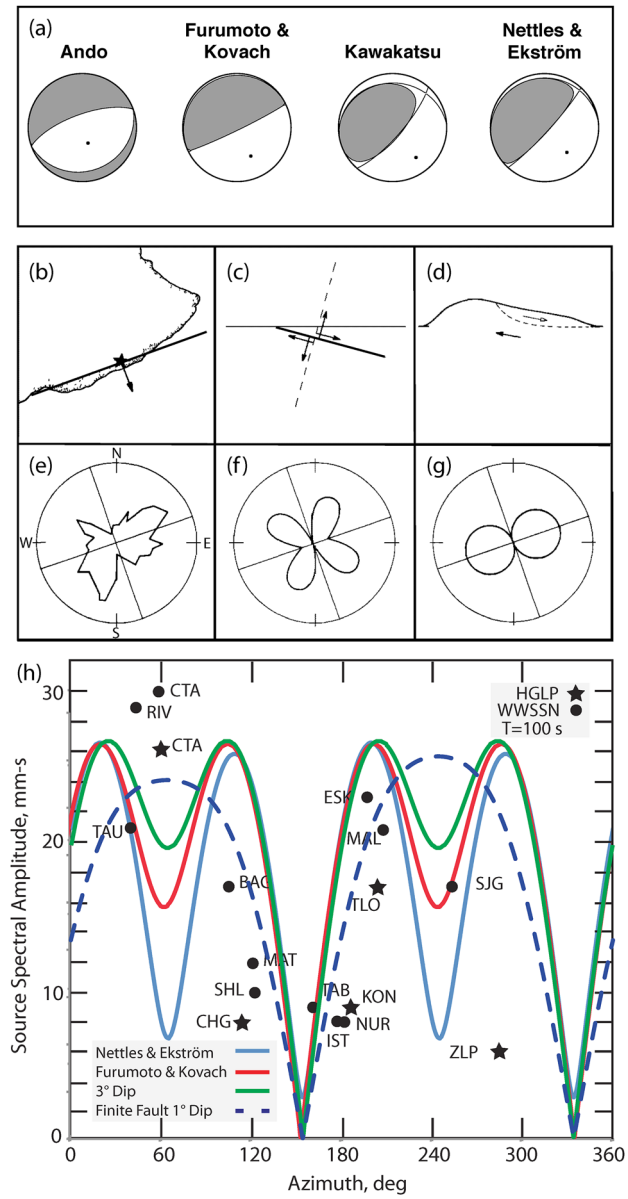

Figure 2. Summary of teleseismic point-source model constraints for the 1975 Kalapana, Hawaii, earthquake. (a) Lower hemisphere focal mechanism projections for the fault models of Ando (1979) and Furumoto and Kovach (1979), and centroid-moment-tensor point-source solutions of Kawakatsu (1989) and Nettles and Ekström (2004) (after Nettles & Ekström, 2004). (b) Epicenter of the 1975 earthquake, with the trend of the fault plane solution from Ando (1979) and direction of the observed maximum coastal displacement (vector). (c) Cross-section through the double-couple source geometry for the normal fault solution of Ando (1979), with the dashed line indicating the auxiliary nodal plane. (d) Single reaction force (lower vector) for a shallow slump model. (e) Observed Love wave radiation pattern from Ando (1979). (f) Theoretical Love wave radiation pattern for the mechanism of Ando (1979) with a dip of 10°. (g) Theoretical Love wave radiation pattern for the single force model like panel (d) with force strike of 330°. (b)–(g) Modified from Eissler and Kanamori (1987). (h) Observed (symbols) and theoretical 100 s period Love wave source spectra (curves) for the 1975 Kalapana event. Observed data are from Eissler and Kanamori (1987). The blue curve is for the CMT solution of Nettles and Ekström (2004). The red curve is for the mechanism of Furumoto and Kovach (1979) with a dip of 4°. The green curve is for a thrust with strike 244°, dip 3°, and rake 90° with $M_0 = 9.9 \times 10^{20}$ Nm. The dashed curve is for a bilateral rupture model extending 32 km along positive strike direction and 24 km along negative strike direction with strike 244°, dip 1°, rake 90° and $M_0 = 16 \times 10^{20}$ Nm, with rupture velocity of 1.5 km/s and 30 s particle dislocation time from Lay et al. (2018).

thrust-faulting estimates for the 1975 Kalapana long-period seismic radiation are compatible with offshore reflection imaging of the décollement (e.g., Morgan et al., 2003; Park et al., 2007), which indicates ~4° dip toward the island relative to the horizontal. Rigorously accounting for the effects of dipping rock surface and variable water depth above the source requires the 3D calculation of the surface wave excitation, so there is substantial intrinsic uncertainty in the moment estimation.

Geodetic studies have also yielded a range of landslide/slump and décollement faulting interpretations of the 1975 event. Lipman et al. (1985) interpreted the large coastal deformation along the HFZ as evidence for gravitational slumping with up to 3 parallel faults onshore and offshore extending down and flattening at depths of 6–8 km to merge with the décollement. The observed tsunami was attributed to the uplift of the submarine south flank of Kilauea associated with the composite slump movement at the toe. Owen and Bürgmann (2006) find that 7.1 m of slip on a 3° dipping décollement fault segment 41 km long and 41 km wide accompanied by faulting at the Kilauea summit and in the Southwest and East Rift Zones can account well for coseismic deformation along the southeast shore. Their décollement slip model, most of which locates offshore, has a seismic moment of 3.6×10^{20} Nm, with additional on-land faulting increasing the total moment to 4.1×10^{20} Nm. The shallow dip of this model predicts two-lobed Love wave radiation (Figure 2), but there is no indication of whether it can reproduce the tsunami observations.

A scaled-down version of the 1975 Kalapana earthquake occurred along the southeast shore of Hawaii Island on 4 May 2018. Regional strong-motion, broadband teleseismic, and GPS datasets. allow finite fault inversions of the source mechanism to precisely infer the rupture process (e.g., Bai, Ye, et al., 2018; Lay et al., 2018; Liu et al., 2018). The M_W 6.9 to 7.2 earthquake involved northwestward shallowly dipping (2.5°–7.5°) thrust motion during the early stage of the East Rift Zone fissuring accompanying the 2018 Kilauea eruption. The epicenter for the 2018 earthquake is close to that for the 1975 Kalapana event (Figure 1b). Slip of up to 3.5 m occurred offshore on a shallowly dipping thrust fault compatible with being the basal décollement northeast of the large deformation zone in the 1975 event (Bai, Ye, et al., 2018; Kehoe et al., 2019; Liu et al., 2018). This faulting model can account for the tsunami observations at water-level stations and tide gauges from Hawaii Island to Kauai (Bai, Ye, et al., 2018). Coastal landslide was not involved but remains a major concern to local communities and emergency management agencies due to the unpredictability of the potential tsunami impact in addition to the short travel times involved. The 2018 event prompts a reevaluation of the 1975 source process to improve understanding of the tsunami genesis across the archipelago for the development of emergency response plans and mitigation strategies.

As noted above, there have been numerous previous analyses of the seismic and geodetic ground motions for the 1975 Kalapana event, with distinct source representations being proposed. None of the aforementioned seismic and geodetic models have been shown to account for both the near-field tsunami runup and the far-field tide gauge recordings across the archipelago. They also differ in their prediction of the long-period seismic source parameters. Day et al. (2005) did attempt to model the near-field and far-field tsunami observations, but without demonstrating how their models predict geodetic or seismic observations. Here we present a compound faulting model for the 1975 Kalapana earthquake comprised of simplified representations of landslide-like and décollement faulting constrained by general patterns of geodetic and seismic data. Both runup observations along the southeast shore of Hawaii Island and tide-gauge recordings at Hilo, Kahului, and Honolulu provide the primary constraints for iterative refinement of the fault-slip distribution through forwarding tsunami modeling. The goal is to bound the relative contributions of the distinct faulting components to the 1975 tsunami genesis so that tsunami hazard across the archipelago can be related to specific faulting scenarios, supplementing the calibration provided by the much smaller 2018 earthquake and tsunami (Bai, Ye, et al., 2018).

2. Tsunami Modeling and Faulting Representation

NEOWAVE is a proven tool for modeling energetic tsunamis with large bores and runup heights (e.g., Bai, Yamazaki, et al., 2018; Yamazaki et al., 2018). This depth-integrated non-hydrostatic model includes a vertical velocity term that can account for flows over the steep volcanic slopes, period-dependant shoaling of tsunami waves, and dispersion in the deep ocean around the Hawaiian Islands (Bai & Cheung, 2018; Yamazaki et al., 2009, 2011). Figure 1a shows the model region across the major Hawaiian Islands and

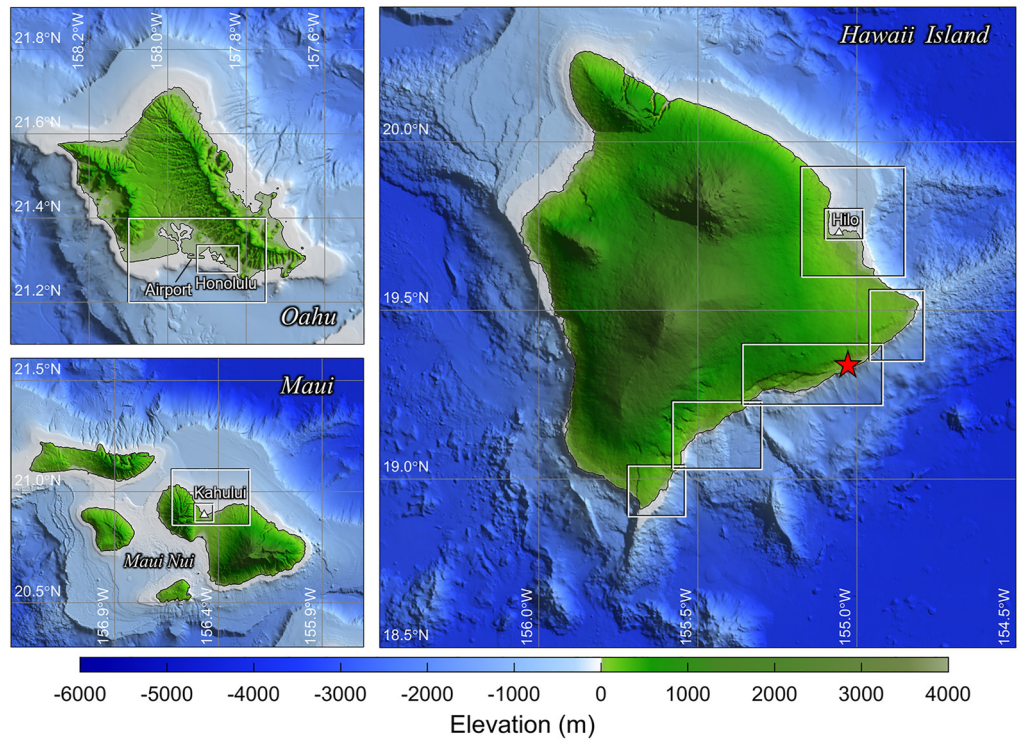

Figure 3. Nested computational grids, digital elevation models, and location maps. Figure 1a shows the coverage of the level-1 grid. The three panels show the level-2 grids and layout of telescopic level-3 and 4 grids in white rectangles. White triangles indicate locations of tide gauge and red star denotes the epicenter of the 1975 Kalapana earthquake.

Figure 3 illustrates the setup of two-way nested computational grids for modeling of the tide gauge and runup records of the 1975 Kalapana tsunami. The level-1 grid covers the entire model region with 30 arcsec (~900 m) resolution to describe tsunami propagation and long-period inter-island standing waves, while the level-2 grids at Oahu, Maui, and Hawaii Island have a higher resolution of 6 arcsec (~180 m) to capture edge waves over the insular shelves and slopes (Cheung et al., 2013). A series of level-3 grids at 1 arcsec (~30 m) resolve nearshore wave processes for runup computation on southeast Hawaii Island. A separate set of level-3 grids at 1.5 arcsec (~45 m) provide transitions to the level-4 computations, which cover Hilo, Kahului, and Honolulu Harbors at 0.3 arcsec (~9 m), for tide gauge signals. The digital elevation model comprises hydrographic survey soundings of the three harbors as well as LiDAR and multibeam datasets with resolutions of 1–4 m and 50 m respectively. The elastic half-space model of Okada (1985) is used to compute the land surface deformation from faulting models. The use of an effective dip angle measured from the average seafloor slope allows differentiation between normal and thrust slip in the soling faults beneath the steep volcanic flank. The computed vertical seafloor displacement is augmented by the horizontal motion of the local slope to define the tsunami excitation (Tanioka & Satake, 1996). The Hawaii tide range is about 0.6 m and the local mean-sea level is used in modeling near and far-field wave processes.

The proposed compound faulting model is constructed to provide a general representation of available seismic and geodetic observations conducive to tsunami excitation. Figure 4a shows the complex aftershock distribution from the 1975 Kalapana earthquake. Activity extends along the shore seaward of the East Rift Zone and further inland along the Southwest Rift Zone and near the Kilauea crater. There is sparse offshore aftershock activity along this entire stretch of shoreline, and location uncertainty tends to increase with distance offshore. Most seismicity near the East Rift Zone locates below land at depths of 7–10 km, with almost all events having P-axes trending about 150° and T-axes trending near 330° (Crosson & Endo, 1982). This region has a mix of shallowly dipping thrust and normal faulting first-motion focal mechanisms, with substantial uncertainty in the plunge of the steeply dipping planes. Harvey and Wyss (1986) infer a distribution of strong-ground motion sources inland along most of the aftershock zone with an overall low ~0.8 km/s rupture velocity toward the southwest, but the limited observations do not provide a detailed slip

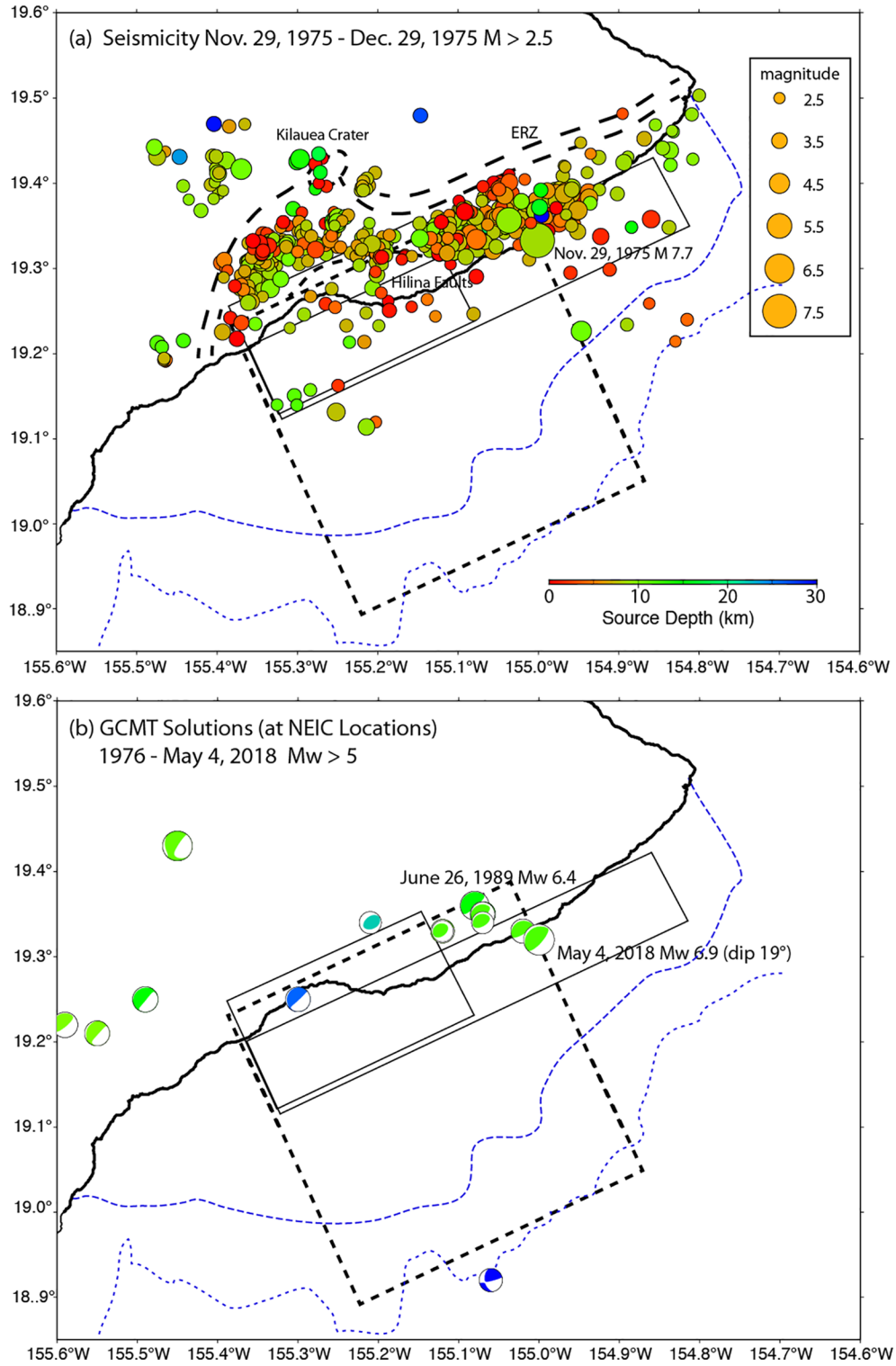

Figure 4. Geometric constraints on fault models. (a) Aftershocks of the 1975 Kalapana earthquake during a 1-month period with magnitude ≥2.5 in the USGS-NEIC ComCat catalog. Symbols are scaled proportionally to the seismic magnitude and color-coded for source depth. East Rift Zone, Southwest Rift Zone, Hilina Fault System, and Kilaua Crater are labeled. (b) Global centroid-moment-tensor solutions for events larger than M_W 5.0 from 1976 to May 4, 2018. Black rectangles delineate the décollement faulting models from Owen and Bürgmann (2006) (dashed line) and the preferred compound model (light solid lines). Bold and fine dashed blue lines indicate bathymetric extents of the smooth and crumpled bench margins of the island.

distribution on the fault. Denlinger et al. (1995) relocated all events from 1970 to 1989 and suggest that the 7–10 km deep activity is on the low-angle décollement plane proposed by Got et al. (1994) that extrapolates to an offshore bench 30–40 km from the shore. Available global centroid-moment-tensor focal mechanisms for events with $M_W \geq 5.0$ support a shallowly dipping thrust geometry along the shore (Figure 4b), but the resolution of fault dip and the corresponding seismic moment is limited. We initially considered a 41 km by 41 km décollement fault with a 7.1 m uniform slip from Owen and Bürgmann (2006) that extends out to the deformed bench far beyond the offshore aftershocks as shown in Figure 4. Tsunami calculations for this model show over-prediction of the initial wave height at the Hilo tide gauge by 59% and a factor of 2 under-prediction of the peak runup in the HFZ region (Figures S1 and S2 in Supporting Information S1), indicating the need for a narrower décollement fault and a second, localized tsunami source.

The sparsity and imprecise location of the offshore seismicity make it difficult to infer the distribution of offshore slip during the 1975 event, particularly its up-dip (seaward) extent. Bai, Ye, et al. (2018) encountered a similar situation for the 2018 M_W 7.2 earthquake, with few offshore aftershocks occurring in the region where large mainshock slip is required to account for the observed tsunami. They interpreted the lack of offshore aftershocks as an indication of substantial stress relaxation in large-slip zones, possibly with aseismic deformation occurring up-dip toward the toe of the flank. Detailed analysis of the aftershock sequence for the 2018 event reveals a second sub-horizontal band of seismicity 3.5 km deep along the HFZ (Lin & Okubo, 2020), which was proposed as a structure that may have also been active in the 1975 rupture, possibly involving block motions connecting to the surface ruptures of the Hilina faults (e.g., Cannon et al., 2001). We explore faulting models for offshore décollement rupture extending along the length and width of the coastal aftershock distribution from the 1975 earthquake, together with landslide-like block faulting from the HFZ to offshore as inferred from the 2018 earthquake. Figure 4 shows outlines of the preferred compound faulting model along with the starting décollement model from Owen and Bürgmann (2006) to demonstrate the wide parameter space considered. With the primary goal being to account for the tsunami observations, the considered faulting models do not include deep slip on the décollement located under land or the faults producing seismicity near the Kilauea crater and in the rift zones inland from the shore to avoid over parameterization of the source model.

The observed ground deformations associated with the 1975 Kalapana earthquake, as summarized in Figure 5a, provide additional guidance for model refinement. The horizontal and vertical displacements are largest at the shore along the HFZ with a maximum of ~8 m southeast and 3.5 m downward, respectively. Deformation decreases northeast of the epicenter and inland from the shore but maintains a relatively uniform direction to the southeast. Owen and Bürgmann (2006) model the localized deformation around the Kilauea crater and discuss the difficulty of estimating the actual coseismic deformation from trilateration, leveling, and tilt data due to the irregular data sampling, complexity of multiple parallel strands of faulting, and prior swarm/eruption activity in December 1974. Coastal down drop and possible contribution from additional near-surface offshore faults (e.g., Day et al., 2005; Lipman et al., 1985) likely enhance the measured coastal horizontal deformation. We do not attempt to match the peak displacements right along the shore and the deformation near the Kilauea crater in our elastic modeling. It is, however, necessary to subdivide the décollement and landslide faults into uniform-slip segments to provide additional degrees of freedom for simultaneously matching the overall spatial pattern of horizontal and vertical deformations as well as the tide gauge and coastal runup observations. The data constraints are insufficient to produce a kinematic model, but likely the décollement rupture progresses in a southwesterly direction from the hypocenter with a low rupture velocity and total duration of about 72 s (Harvey & Wyss, 1986; Nettles & Ekström, 2004).

3. Compound Faulting Model

A wide range of décollement and landslide fault dimensions was explored to determine the sensitivity of the geodetic and tsunami data to the fault segmentation. The width of the offshore décollement slip was progressively narrowed from the starting model to reduce overprediction of the tide gauge signals and accommodate the contribution from the landslide-like faulting needed to match the near-field runup. We use the geodetic information to guide the along-strike length of the landslide component and tsunami modeling to infer the offshore slip magnitude and extent on the extrapolated fault. Table 1 lists the geometric parameters for the preferred compound faulting model involving seven segments, and Figures 5a and 5b provide the

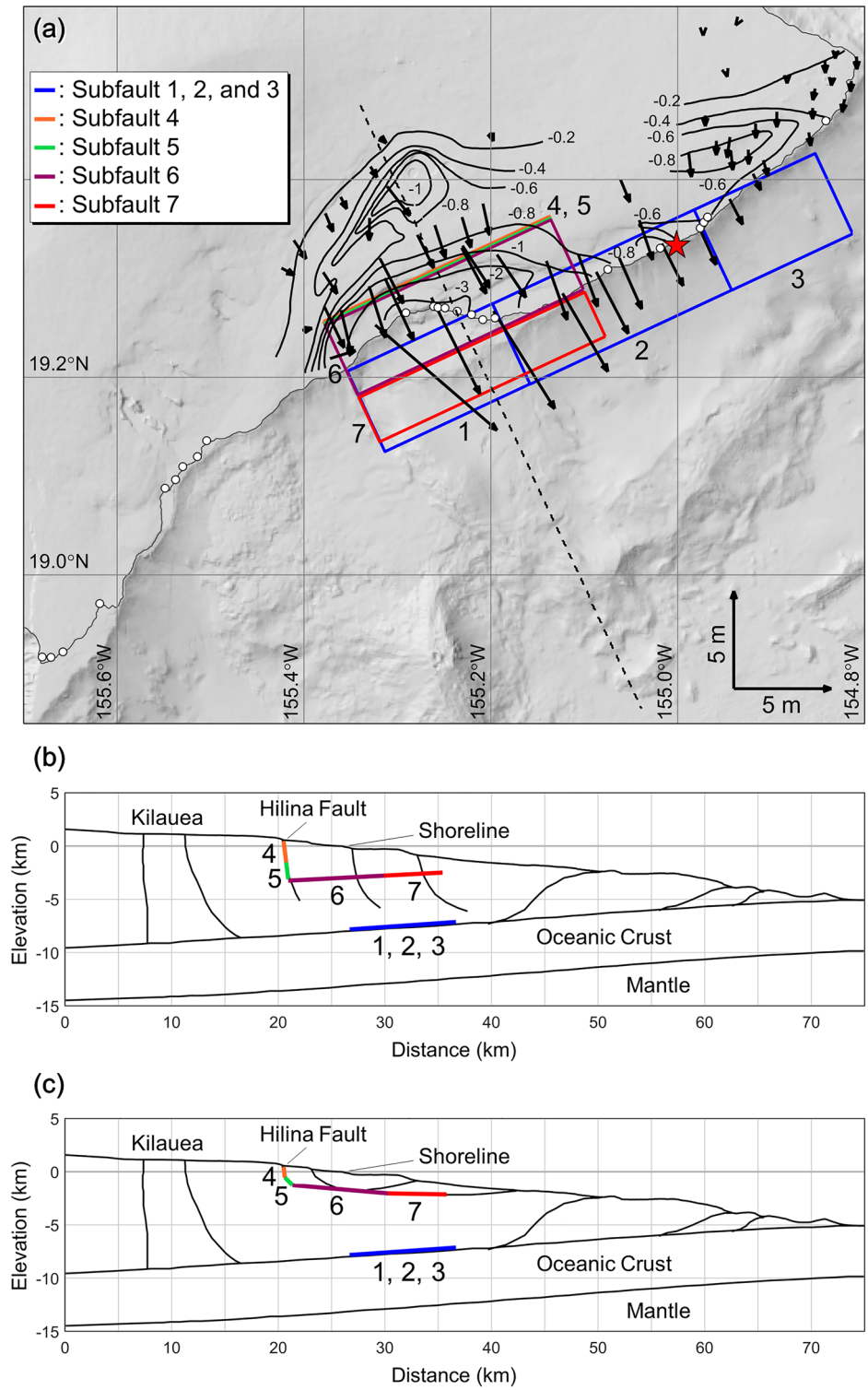

Figure 5. Schematics of compound faulting models for the 1975 Kalapana, Hawaii, earthquake and landslide. (a) Two-fault model and observed coseismic ground deformations from Ma et al. (1999), who in turn derived the data from Lipman et al. (1985). Red star denotes the epicenter and white circles indicate locations with observed runup from Tilling et al. (1976). Cross-section of décollement faulting with (b) Hilina landslide block faulting involving 3 km deep interface (Lin & Okubo, 2020). Background fault lines were adapted from Cannon et al. (2001) and Owen and Bürgmann (2006), and (c) Hilina shallow landslide faulting (Eissler & Kanamori, 1987; Owen & Bürgmann, 2006; Swanson et al., 1976).

Table 1
Fault Parameters of the Preferred Compound Model of Décollement and Hilina Landslide Block Faulting

Subfault No.	D_0 (m)	Lat$R$ (°N)	Lon$R$ (°W)	dR (km)	L (km)	W (km)	φ (°)	δ_h (°)	δ_g (°)	δ (°)	λ (°)
1	7.0	19.19326	155.15811	5.7	18	10.0	245	4	6	10	90
2	8.0	19.28815	154.94223	4.7	25	10.0	245	4	6	10	90
3	4.5	19.34512	154.81265	3.7	15	10.0	245	4	6	10	90
4	4.0	19.25660	155.37923	0.0	28	2.0	65	83	9	74	270
5	4.0	19.25461	155.37825	2.0	28	1.6	65	83	9	74	270
6	4.0	19.28603	155.09951	1.6	28	9.0	245	3	9	12	90
7	10.0	19.24126	155.07748	0.8	28	5.5	245	3	6	9	90

Note. See Yamazaki et al. (2011) for details. D_0: Slip; Lat$R$: Latitude at reference point; Lon$R$: Longitude at reference point; dR: Depth at reference point (updip edge of subfault nearest to ground surface); L: Length; W: Width; φ: Strike angle; δ_h: Dip angle relative to horizontal; δ: Dip angle relative to ground surface; δ_g: Average angle of ground surface relative to horizontal; λ: Rake angle.

plan view and cross section to illustrate the construct. The preferred model represents an optimal solution from over 150 realizations of fault geometry and slip distribution. A notable feature is that the along-dip width of the décollement slip zone is only 10 km; much less than the 41-km wide fault of the starting model. The first two décollement subfaults together extend 43 km along strike, comparable to the starting model. Guided by the geodetic data, we extend the décollement fault 15 km to the northeast, overlapping the 2018 M_W 7.2 rupture area. The décollement faulting is complemented by a landslide block model with steeply dipping normal faulting from Hilina Pali down to a 3.5 km deep shallowly dipping fault extending offshore (Lin & Okubo, 2020). We also converged on an alternate compound model with the same décollement fault, but a shallow (<1 km deep) landslide-like fault geometry closer to the surface (Table S1 in Supporting Information S1; Figure 5c), motivated by the slump model concept of Eissler and Kanamori (1987). Other than the seismogenic feature at ~3.5 km depth along the base of the landslide block, the specific geometries of fault surfaces in these block and slump models are not tightly constrained by direct observations and are simple elastic dislocation representations of what was possibly a complex landslide and run-out process.

Figure 6 compares the observed coseismic vertical and horizontal ground displacements with predictions from the preferred décollement, Hilina landslide block, and combined compound faulting (Figure S3 in Supporting Information S1 shows very similar comparisons for the final Hilina shallow landslide model). The décollement fault gives a reasonable representation of the regional deformation surrounding the HFZ. The slip reduces along-strike from 7 and 8 m in subfaults 1 and 2 to 4.5 m in subfault 3 to the east (Figure 5, Table 1), where the 2018 earthquake occurred with ~3 m average slip (Bai, Ye, et al., 2018). This suggests significant residual strain not released by the 1975 Kalapana event in the eastern fault zone was available for the 2018 rupture. The on-land portion of the landslide block faulting provides an overall account of the observed deformation near the HFZ. The 4-m slip in subfaults 4–6 captures the escarpment from normal faulting deformation along the hillside and together with the décollement fault reproduces the up to ~5 m seaward movement of the coastal land. The slip increases to 10 m in subfault 7 to account for the large subsidence extending to the shore and to capture tsunamigenic effects of strong deformation and possible run-out of the landslide at the toe. The landslide block and décollement faults are almost aligned at their offshore boundaries. This is a necessary condition and an important constraint to reproduce the observed runup with the amount of slip required to fit the geodetic and tide gauge records. Questions about the actual dislocations on the landslide faults versus possible run-out effects of slumping arise primarily from the approximation of the complex landslide deformation with a simplified linear elastic model but should have secondary effects in the resulting tsunami.

The compound faulting model with simplified, uniform-slip segments is not intended to account for non-tsunamigenic localized deformations. Extension of the décollement fault below land along with locally augmented slip and implementation of separate fault models at the Kilauea crater and East Rift Zone can help reproduce the subsidence associated with the caldera collapse and the large horizontal displacement immediately east of the HFZ (Owen & Bürgmann, 2006). The compound faulting model also does not

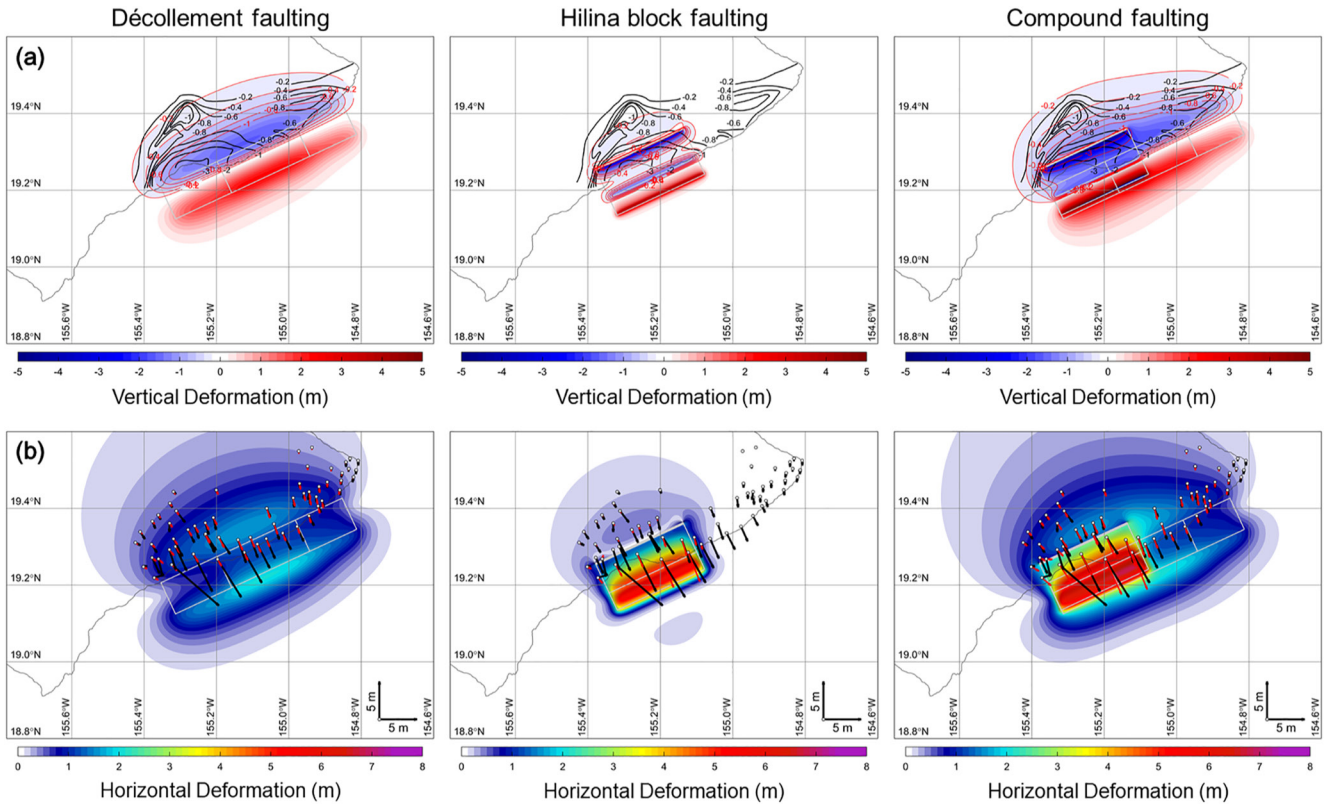

Figure 6. Comparison of observed coseismic ground deformations from Ma et al. (1999) with model results from décollement, Hilina landslide block, and compound faulting in the preferred model. (a) Vertical displacement. Contour lines and color patterns denote recorded values and model results. (b) Horizontal displacement. Black vectors denote recorded values; red vectors and color patterns represent model results.

provide a detailed account for the large and irregular motions immediately west of the HFZ. The observed displacements somewhat inland along the principal Hilina scarp are much more uniform in direction and the contoured displacement field is strongly suggestive of relatively uniform deformation from the landslide block even though there are several curved scarps in the system (Figure 1b). We keep the description of the shallow Hilina faulting simple as there is almost no constraint on the downward extension of the geometry, and there are also multiple surface disruptions in the system that cannot be reasonably modeled with any confidence in downward extrapolation. The large and irregular motions near the western end of the landslide block are likely manifestations of shallow slumping that is subject to local enhancements and rotations in the shallow crustal block along Hilina Pali, but the connection to offshore faulting is not at all clear for exploration in the iterative model process. The tsunami generation is not expected to be sensitive to details of shallow rapid rake or strike variations along the shore or to localized deformation on land.

The total seismic moment, assuming a 30 GPa rigidity is 2.07×10^{20} Nm (M_W 7.5) for the preferred compound faulting model. Of this total 1.2×10^{20} Nm is from the décollement, much lower than the corresponding 3.58×10^{20} Nm for the décollement slip in the model of Owen and Bürgmann (2006), which has a larger rupture area extending further offshore (Figure 4), where no resolution of slip is actually provided by the geodetic data. The discrepancy is partly made up for by the seismic moment in the landslide block component (0.89×10^{20} Nm) or that in the shallow landslide model (0.83×10^{20} Nm). The seismic moment of the compound model is also lower than those given in the caption for the models in Figure 2h, as is also true for the model of Owen and Bürgmann (2006). Using excitation functions for normal modes computed for the PREM Earth model (Dziewonski & Anderson, 1981), far-field 100-s period Love wave spectra are computed for the individual components assuming spherically symmetric model excitation functions and summed for total radiation of the compound faulting model (Figure S4 in Supporting Information S1), showing predominantly two-lobed Love-wave radiation as observed for the event. The small dips of the offshore faults would require several times larger seismic moment to match the observations. This may be mitigated by using dip

relative to the seafloor, which reduces the seismic moment needed to fit the observations but will tend to produce four-lobed Love-wave radiation for a 1D calculation. An accurate estimate of the long-period seismic wave excitation for a medium with surface topography and vanishing ocean layer requires a fully 3D calculation, which is beyond the scope of the current study.

4. Modeled Tsunami and Observations

Comparison of the modeled tsunami with both tide gauge and coastal runup records is the primary factor in selecting the preferred compound faulting model. Figure 7 provides snapshots of free surface elevation near the tsunami source and across the Hawaiian Islands to illustrate the complex wave processes (See Movies S1 and S2 for the full sequence). The offshore seafloor movement generates radiated waves with an oblong pattern associated with the initial pulse length and width. The resulting long and short period waves, which propagate in the long-shore and cross-shore directions from the source, also depend on the water depth beneath the initial pulse. Meanwhile, the initial drawdown of ∼2 m near the Kalapana shore produces an upswing of the local free surface. The rising water coincides with the arrival of the initial crest from the short-period radiated waves. The high-resolution computation shows that the combined wave action produces an energetic surge to 17.3 m on the steep volcanic slope within 3 min after the earthquake. This is followed by a large drawdown to 15.7 m below mean sea level about 3 min later. The non-hydrostatic properties of NEOWAVE become instrumental in describing the vertical flow dynamics (Bai et al., 2018). Away from the source, the peak surge at the shore occurs well after the long-period arrivals, indicating edge wave excitation from the cross-shore, short-period energy. The enduring shore-bound short-period oscillations gradually spread around the island. The long period waves can more effectively wrap around to the west and north-facing shores before converging at the northern tip and bouncing off to the interconnected insular shelves known as Maui Nui (Figure 3). Meanwhile, refraction-diffraction of the faster propagating offshore waves around Hawaii Island reaches Maui Nui from the north and south. The shallow shelf complex traps a significant amount of energy from the tsunami with leakage to Oahu via Penguin Bank (Figure 1a). The narrow insular shelves of Kauai and Niihau are not connected to the rest of the islands with tsunami excitation primarily from the offshore propagation, which is much attenuated due to the distance from the source.

The Hilo, Kahului, and Honolulu tide gauges in operation during the tsunami were stilling wells with the water level traced on a rotating drum (Cox, 1980). Figure 8 compares the processed tide gauge records with the model results for the décollement, Hilina landslide block, and compound faulting. The computed waveforms match the recorded arrival times of the 2018 tsunami with an overlapping source (Figure S5 in Supporting Information S1), but require a shift of 2.5–6.5 min to align with the recorded arrivals in the 1975 event. Clock errors of ±2 min were estimated for the tide gauges; the timing discrepancy of 6.5 min at Hilo is substantial for a local event and might be attributed to instrumentation errors from shaking by the earthquake (Cox, 1980). The model produces distinct tsunami waveforms from the décollement and landslide-like faults at the three locations. The model results at Hilo show sequential arrivals of long and short period signals associated with waves propagating directly from the source and edge waves arriving via the insular shelf. The wave periods primarily reflect the length and offshore extent of each fault system. The compound faulting model gives a good description of the initial long-period arrivals but overestimates the short-period signals of ∼6 min in the subsequent oscillations primarily from the landslide-like faulting. The wave period is within the applicable dispersion range of NEOWAVE even for the deep ocean (Bai & Cheung, 2016). The discrepancy might be due to the elastic approximation of the landslide deformation and/or low recording intervals used at the time. In addition, stilling-well tide gauges are known to damp and lag short-period tsunami signals (e.g., Satake et al., 1988). The short-period components, which are mostly trapped edge waves on the Hawaii Island shelves, become much attenuated in the far field. The long-period waves of ∼20 min originating predominantly from the décollement fault give very good agreement with the records at the Kahului tide gauge, but overestimate the later arrivals at Honolulu, likely due to local resonance caused by the adjacent airport runway (See Figure 3), which was only partially built in 1975.

The tide gauge records have validated the long-period waves generated by the décollement and landslide-like faults giving overall confidence in the respective length, offshore extension, and overall slip. The good agreement of computed and recorded runup on southeast Hawaii Island in Figure 9 lends support to the amplitude of the short-period waves directly from the source. The combined seafloor deformation from

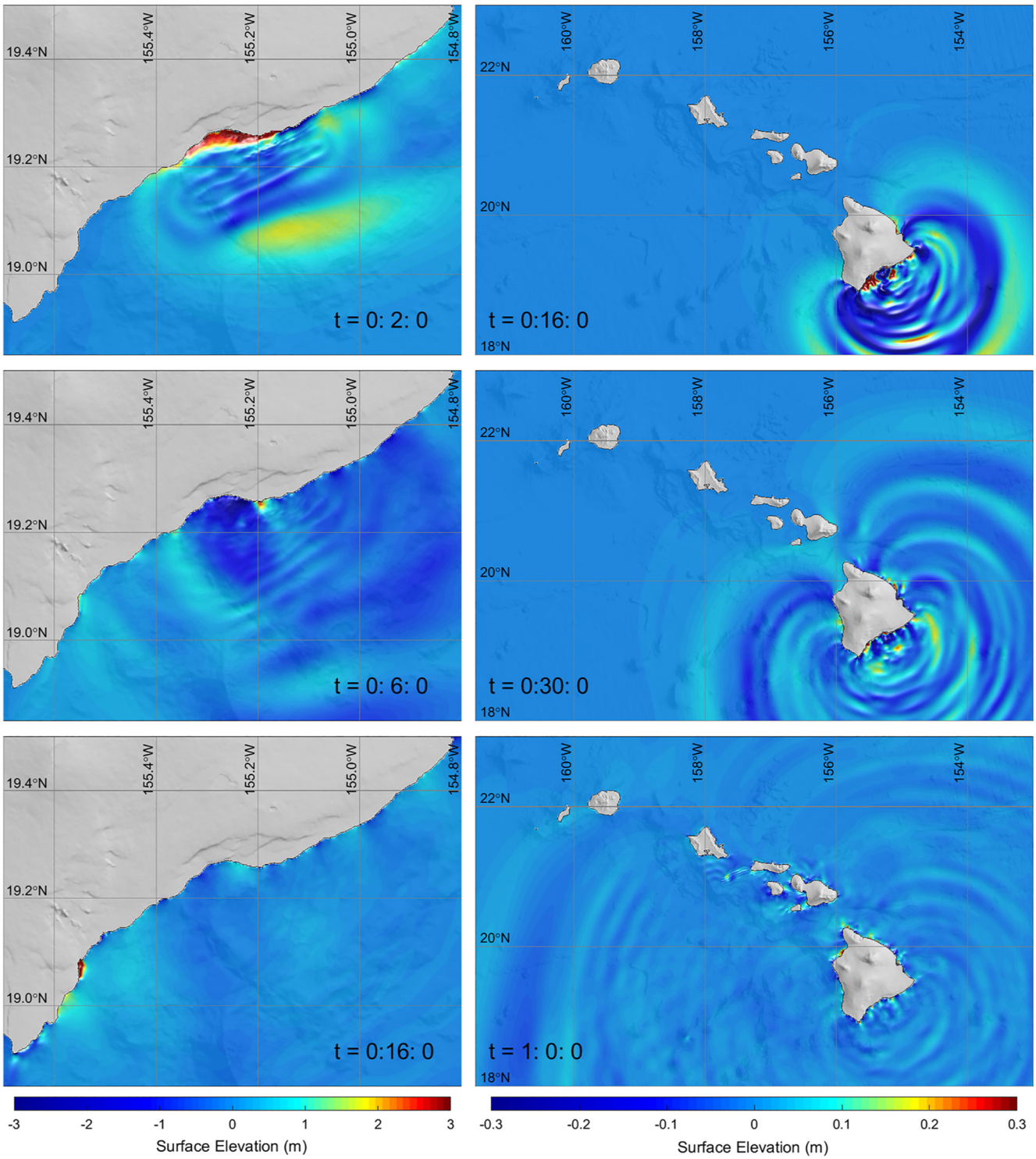

Figure 7. Snapshots of computed free surface elevations near the tsunami source (left column) to demonstrate near-field wave processes and around the major Hawaiian Islands (right column) to illustrate long-period tsunami waves generated at the source and subsequent short-period signals via coastal edge wave formation. Time t is in hour, minute, and second after earthquake initiation.

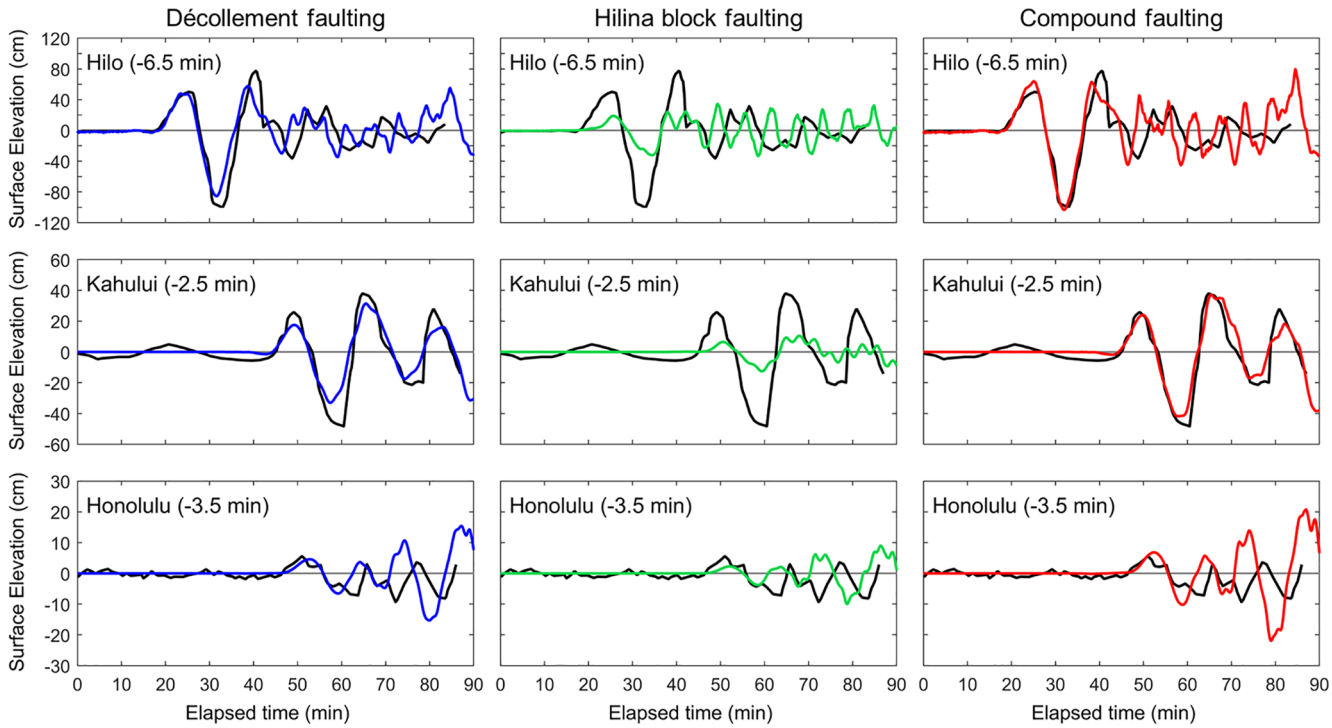

Figure 8. Comparison of tide gauge records (black) with model results from décollement (blue), Hilina landslide block (green), and compound (red) faulting in the preferred model. The recorded time series were digitized from Ma et al. (1999), who in turn post-processed the data from Cox (1980). The computed time series has been shifted by the indicated amount in each panel to align with the recorded arrival.

the two faults generates an initial sea surface elevation of 6.8 m facing the Kalapana shore. The short-period waves from the two faults are in phase and their superposition results in the maximum computed runup of 17.3 m. The runup to the southwest and northeast of the HFZ is primarily a result of short-period edge wave excitations and is substantially smaller than the sum from the two components due to timing offsets. The runup records on southeast Hawaii Island, which provide a profile of the tsunami source intensity, are critical in resolving the slip distribution in the compound faulting model. Also shown in Figure 9 are the wave amplitudes from the décollement, Hilina landslide block, and compound faulting that provide insights into the local tsunami hazards. The tsunami waves generated by the earthquake and landslide have varying properties and impacts along the Hawaiian Islands. Southeast Hawaii Island is the hardest hit due to its proximity to the source as well as shoaling and reflection of the tsunami waves from the steep near-shore slope. The long-period tsunami waves from the décollement fault wrap around headlands to produce secondary impacts on the east and west-facing shores. The waves reach the rest of the island chain through diffraction of the offshore propagating waves and edge waves over the interconnected insular slopes and shelves. The tsunami impacts from the landslide are limited primarily to Hawaii Island because the shorter-period edge waves have insufficient length to clear the channel via the shelves. The compound faulting with shallow landsliding provides very similar comparisons with the tide gauge and runup records (Figures S6 and S7 in Supporting Information S1).

The sensitivity of the computed tide gauge signals and runup heights is well established through the iterative refinement of fault geometry and slip distribution that leads to the preferred compound faulting model. There is a rather limited parameter range that allows good simultaneous reproduction of the recorded tsunami runup and tide gauge signals while corroborating the general pattern of the geodetic observations. The initial arrival at the Hilo tide gauge is most sensitive to the offshore extent of the décollement fault due to the wrap-around of the diffracted waves directly from the source. The computed initial wave height, which includes both components of the compound faulting model, is 11% higher than the recorded value. The runup records from Tilling et al. (1976) cover the entire southeast shore of Hawaii Island. The localized large runup near the HFZ is sensitive to the landslide block movement and its alignment with the offshore

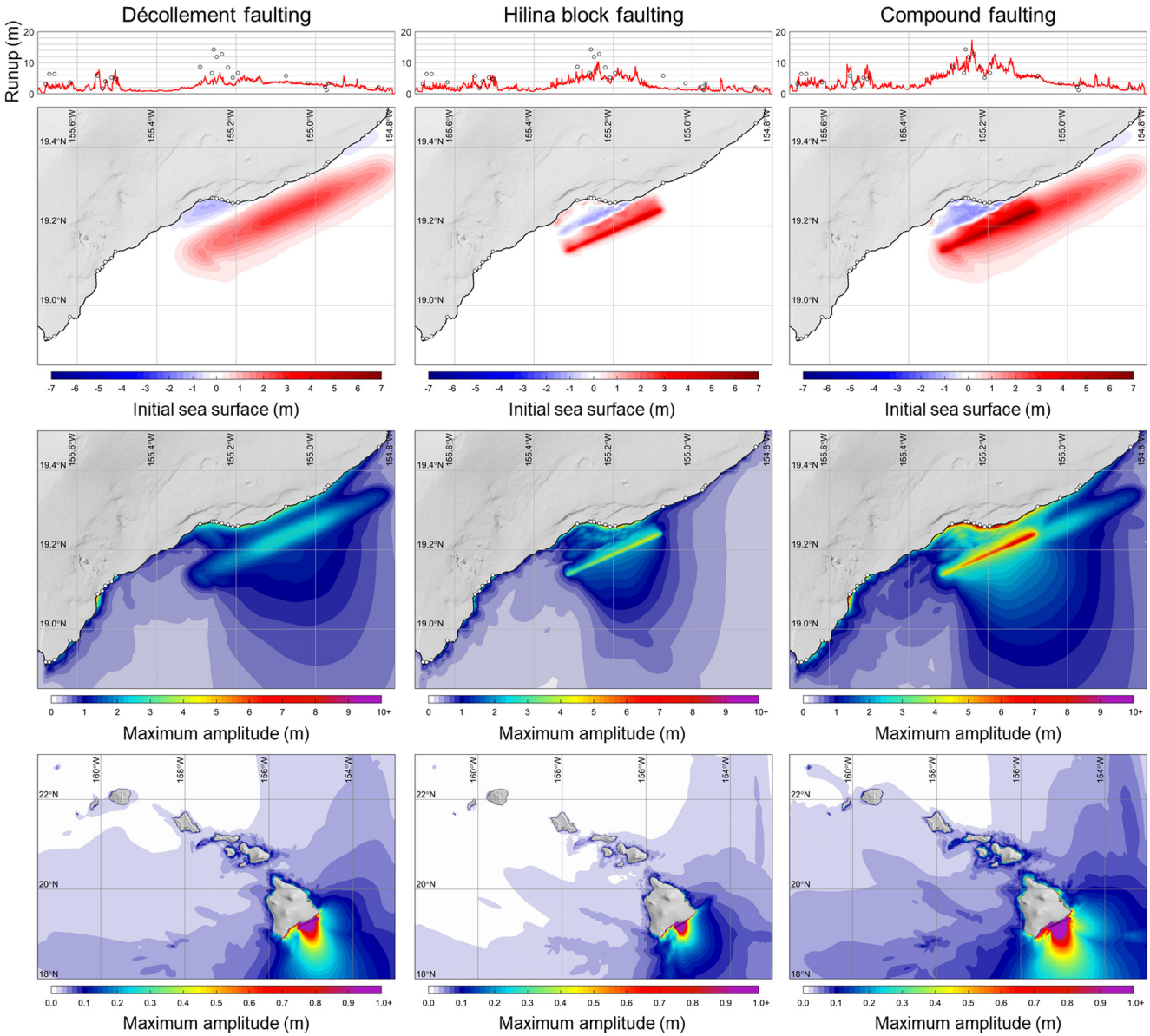

Figure 9. Tsunami runup (top row), initial sea surface (second row), and maximum wave amplitude along southeast Hawaii (third row) and across the island chain (fourth row) from décollement, Hilina landslide block, and compound faulting in the preferred model. White circles indicate tsunami runup and record locations from Tilling et al. (1976) and red lines indicate computed runup from the respective sources. Both the computed and reported runup references the mean sea level.

limit of the décollement fault. The computed maximum runup is saddled between two records and 21% higher than the maximum recorded value. The over-predictions are deemed acceptable due to potential artifacts in the tide gauge records as well as the availability and accessibility of runup evidence in the most remote part of Southeast Hawaii Island. The décollement and landslide fault geometries appear to reach an optimal point as the computed initial wave height and maximum runup do not vary appreciably within ±10% variation of the fault dimensions for the given slip distribution in Table 1. In contrast, the computed wave height and runup increase by 8.9% and 6.6% and decrease by 8.6% and 10.0% for ±10% slip variation in the preferred model.

5. Discussion and Conclusions

The source mechanism for the 1975 Kalapana event is not well constrained by available observations as evident by the wide range of proposed faulting models in the literature. Having a high-resolution digital elevation model and a non-hydrostatic tsunami code allows effective use of the coastal runup and tide gauge records along with the seismic and geodetic observations to infer a compound model involving simplified décollement and landslide block faulting. The solution is far from unique as the compound model with an alternate shallow-landslide component can reproduce the geodetic and tsunami observations comparably well. There can also be some trade-off between the two faulting components. In the limiting case, a décollement faulting model with sufficient coverage and complexity in parameterization might achieve comparable agreement to at least some of the observations by itself. This will require roughly a threefold increase of the décollement slip immediately offshore of the HFZ to make up for the seafloor deformation from the landslide component of the compound model, as inferred from Figures 6 and 9. The very large and localized décollement slip beneath the mobile flank will lead to an unlikely rupture scenario for the event. The landslide block faulting, which is consistent with a sub-horizontal band of seismicity in the 2018 aftershock sequence (Lin & Okubo, 2020), provides a physically more sensible way to account for the large localized seafloor deformation, complementing equally probable décollement faulting in describing the source processes conductive to tsunami excitation.

Our compound faulting model does not include the timing of the rupture processes as there is no direct observational control on the offshore kinematics. The below-land portion of the décollement rupture likely propagated from the epicenter southwestward with a total duration of around 72 s (Harvey & Wyss, 1986; Nettles & Ekström, 2004). Inclusion of subfault timing in the décollement faulting process assuming unilateral rupture expansion will slightly steer the offshore propagating waves to the south and delay the initial peak and lengthen the initial wave at the Hilo tide gauge by up to ~1 min. However, the rupture propagation will likely have secondary effects on the long-period initial wave of ~20 min at the Hilo tide gauge. Delaying the onset of the landslide by a few minutes or implementing it over a finite duration may improve the match with the later edge wave arrivals of ~6 min period at the expense of the initial long-period wave. The timing offset will reduce the coastal runup near Kalapana as the onshore initial waves from the landslide and décollement faults will likely be not aligned, although this can be compensated by increasing the slip on the faults or extending the décollement fault offshore. Due to filtering by the stilling-well tide gauge, the recorded short-period waves do not have the precision to reliably resolve the temporal evolution of the source processes. The good reproduction of the initial wave by the compound faulting model suggests that the two faults likely failed at about the same time as assumed in this study. Such a scenario is more probable for the preferred landslide block faulting than for the alternate shallow-landslide component based on the slump model concept of Eissler and Kanamori (1987).

The preferred compound faulting model for the 1975 Kalapana earthquake is compatible with the overall extent and direction of land deformation measurements and with the general distributions of aftershock activity and nearshore focal mechanisms. The elastic, segmented fault-slip approximation of landslide block movement and décollement rupture is not intended to account for localized deformation from volcanic and rift zone activities or shallow slumping on land. Our emphasis has been on fitting the tsunami signals with conservative, primarily offshore faulting, and there is some under-prediction of geodetic deformation close to the shore, which could be reduced by having slip extending deeper under the land on the décollement. We explored such models, finding that there is minor influence on the coastal runup and tide gauge waveforms, but given the concerns about the coastal deformation observations noted by Owen and Bürgmann (2006), we present the models here as effective offshore compound faulting representations of the tsunami excitation. As a result, the preferred model represents the tsunamigenic portion and a lower bound estimate of the seismic moment. This conservative approach provides a robust basis and a scalable scheme to assess tsunami hazards along the Hawaiian Island chain from a local source.

The active deformation of southeast Hawaii Island presents one of the key sources of tsunami hazard for the island chain. Thrust faulting on the shallowly dipping décollement associated with the lateral spreading of the mobile flank continues to pose a statewide tsunami hazard, as manifested in the 1975 and 2018 earthquakes. The hazard for a local tsunami along the southeast shore is enhanced by the possibility of landsliding and/or slumping from the Hilina Fault Zone. For the 1975 earthquake, the offshore landslide appears to

have caused twice as much local runup as the décollement slip, but secondary contributions to the far-field tsunami. It is not known with certainty whether the 1868 Ka'u earthquake involved any landslide contribution to the tsunami. The 1868 runup distribution around Hawaii Island is comparable to the 1975 event with similar peak values at very nearby locations (Tilling et al., 1976). Although the 1868 earthquake has a considerably larger magnitude and décollement faulting alone may have been involved, a Hilina landslide component cannot be ruled out given the observed tsunami pattern. While the inundation potential is much reduced beyond Hawaii Island, hazardous coastal currents might interfere with maritime operations and damage harbor facilities. The compound faulting model presented here thus provides a proxy to describe local and statewide tsunami hazards for large earthquakes along the southeast shore of Hawaii Island.

Data Availability Statement

The hydrographic, LiDAR, and multibeam survey datasets for the Hawaiian Islands are available respectively through the US Army Corps of Engineers Honolulu District, National Oceanic and Atmospheric Administration (https://coast.noaa.gov/dataviewer/#/lidar/search/), and University of Hawaii (http://www.soest.hawaii.edu/HMRG/multibeam/index.php). The geodetic, tide gauge, and runup data are available through Ma et al. (1999) and Tilling et al. (1976).

Acknowledgments
Y. Yamazaki and K. F. Cheung received support for the local tsunami hazard assessment from the National Oceanic and Atmospheric Administration (Grant NA19NWS4670012) and Thorne Lay's earthquake research is supported by National Science Foundation (Grant EAR1802364). The authors thank the two anonymous reviewers for their constructive remarks that have improved the organization and discussion of the model results in this study. SOEST Contribution No. 11419.

References

Ando, M. (1979). The Hawaii earthquake of November 29, 1975: Low dip angle faulting due to forceful injection of magma. *Journal of Geophysical Research*, *84*, 7616–7626. https://doi.org/10.1029/jb084ib13p07616

Bai, Y., & Cheung, K. F. (2016). Hydrostatic versus non-hydrostatic modeling of tsunamis with implications for insular shelf and reef environment. *Coastal Engineering*, *117*, 32–43. https://doi.org/10.1016/j.coastaleng.2016.07.008

Bai, Y., & Cheung, K. F. (2018). Linear shoaling of free-surface waves in multi-layer non-hydrostatic models. *Ocean Modelling*, *121*, 90–104. https://doi.org/10.1016/j.ocemod.2017.11.005

Bai, Y., Yamazaki, Y. Y., Cheung, K. F., & Cheung, K. F. (2018). Amplification of drawdown and runup over Hawaii's insular shelves by tsunami -waves from mega Aleutian earthquakes. *Ocean Modelling*, *124*, 61–74. https://doi.org/10.1016/j.ocemod.2018.02.006

Bai, Y., Ye, L., Yamazaki, Y., Lay, T., & Cheung, K. F. (2018). The 4 May 2018 M_W 6.9 Hawaii Island earthquake and implications for tsunami hazards. *Geophysical Research Letters*, *45*, 11040–11049. https://doi.org/10.1029/2018GL079742

Borgia, A. (1994). Dynamic basis of volcanic spreading. *Journal of Geophysical Research*, *99*, 17791–17804. https://doi.org/10.1029/94jb00578

Borgia, A., & Treves, B. (1992). Volcanic plates overriding the ocean crust: Structure, and dynamics of Hawaiian volcanoes. *Geological Society Special Publication*, *60*, 277–299. https://doi.org/10.1144/gsl.sp.1992.060.01.18

Cannon, E., Bürgmann, R., & Owen, S. (2001). Shallow normal faulting and block rotation associated with the 1975 Kalapana earthquake, Kilauea volcano, Hawaii. *Bulletin of the Seismological Society of America*, *91*, 1553–1562. https://doi.org/10.1785/0120000072

Chen, K., Smith, J. D., Avouac, J.-P., Liu, Z., Song, Y. T., & Gualandi, A. (2019). Triggering of the M_W 7.2 Hawaii earthquake of 4 May 2018 by a dike intrusion. *Geophysical Research Letters*, *46*, 2503–2510. https://doi.org/10.1029/2018GL081428

Cheung, K. F., Bai, Y., & Yamazaki, Y. (2013). Surges around the Hawaiian Islands from the 2011 Tohoku tsunami. *Journal of Geophysical Research: Oceans*, *118*(10), 5703–5719. https://doi.org/10.1002/jgrc.20413

Cox, D. C. (1980). *Source of the tsunami associated with the Kalapana (Hawaii) earthquake of November 1975. Joint Institute for marine and Atmospheric research*. University of Hawaii.

Crosson, R. S., & Endo, E. T. (1982). Focal mechanisms and locations of earthquakes in the vicinity of the 1975 Kalapana earthquake aftershock zone 1970–1979: Implications for tectonics of the south flank of Kilauea volcano, Island of Hawaii. *Tectonics*, *1*, 495–542. https://doi.org/10.1029/tc001i006p00495

Day, S. J., Watts, P., Grilli, S. T., & Kirby, J. T. (2005). Mechanical models of the 1975 Kalapana, Hawaii earthquake and tsunami. *Marine Geology*, *215*, 59–92. https://doi.org/10.1016/j.margeo.2004.11.008

Delaney, P. T., Denlinger, R. P., Lisowski, M., Miklius, A., Okubo, P. G., Okamura, A. T., & Sako, M. K. (1998). Volcanic spreading at Kilauea, 1976–1996. *Journal of Geophysical Research*, *103*, 18003–18023. https://doi.org/10.1029/98jb01665

Denlinger, R. P., & Okubo, P. (1995). Structure of the mobile south flank of Kilauea volcano, Hawaii. *Journal of Geophysical Research*, *100*, 24499–24507. https://doi.org/10.1029/95jb01479

Dvorak, J. J., Okamura, A. T., English, T. T., Koyanagi, R. Y., Nakata, J. S., Sako, M. K., et al. (1986). Mechanical response of the south flank of Kilauea Volcano, Hawaii, to intrusive events along the rift systems. *Tectonophysics*, *124*(3–4), 193–209. https://doi.org/10.1016/0040-1951(86)90200-3

Dziewonski, A. M., & Anderson, D. L. (1981). Preliminary Reference Earth Model. *Physics of the Earth and Planetary Interiors*, *25*, 297–356. https://doi.org/10.1016/0031-9201(81)90046-7

Eissler, H. K., & Kanamori, H. (1987). A single-force model for the 1975 Kalapana, Hawaii, earthquake. *Journal of Geophysical Research*, *92*, 4827–4836. https://doi.org/10.1029/jb092ib06p04827

Furumoto, A. S., & Kovach, R. L. (1979). The Kalapana earthquake of November 29, 1975: An intra-plate earthquake and its relation to geothermal processes. *Physics of the Earth and Planetary Interiors*, *18*, 197–208. https://doi.org/10.1016/0031-9201(79)90114-6

Gillard, D., Wyss, M., & Okubo, P. (1996). Type of faulting and orientation of stress and strain as a function of space and time in Kilauea's south flank, Hawaii. *Journal of Geophysical Research*, *101*, 16,025-16,042. https://doi.org/10.1029/96jb00651

Got, J.-L., Frechet, J., & Klein, F. W. (1994). Deep fault plane geometry inferred from multiplet relative relocation beneath the south flank of Kilauea. *Journal of Geophysical Research*, *99*, 15375-15,386. https://doi.org/10.1029/94jb00577

Harvey, D., & Wyss, M. (1986). Comparison of a complex rupture model with the precursor asperities of the 1975 Hawaii Ms = 7.2 earthquake. *PAGEOPH*, *124*, 957–973. https://doi.org/10.1007/bf00879621

Hitchcock, C. H. (1912). The Hawaiian earthquakes of 1868. *Bulletin of the Seismological Society of America*, *2*, 181–192. https://doi.org/10.1785/bssa0020030181

Iverson, R. M. (1995). Can magma-injection and groundwater forces cause massive landslides on Hawaiian volcanoes? *Journal Volcanology and Geothermometry Research*, *66*, 295–308. https://doi.org/10.1016/0377-0273(94)00064-n

Kanamori, H., & Given, J. W. (1981). Use of long-period surface waves for rapid determination of earthquake-source parameters. *Physics of the Earth and Planetary Interiors*, *27*, 8–31. https://doi.org/10.1016/0031-9201(81)90083-2

Kawakatsu, H. (1989). Centroid single force inversion of seismic waves generated by landslides. *Journal of Geophysical Research*, *94*, 12363–12374. https://doi.org/10.1029/jb094ib09p12363

Kehoe, H. L., Kiser, E. D., & Okubo, P. G. (2019). The rupture process of the 2018 M_w 6.9 Hawai'I earthquake as imaged by a genetic algorithm-based back-projection technique. *Geophysical Research Letters*, *46*, 2467–2474. https://doi.org/10.1029/2018GL080397

Klein, F. W., Frankel, A. D., Mueller, C. S., Wesson, R. L., & Okubo, P. G. (2001). Seismic hazard in Hawaii: High rate of large earthquake and probabilistic ground-motion maps. *Bulletin of the Seismological Society of America*, *91*, 479–498. https://doi.org/10.1785/0120000060

Lay, T., Ye, L., Kanamori, H., & Satake, K. (2018). Constraining the dip of shallow, shallowly dipping thrust events using long-period Love wave radiation patterns: Applications to the 25 October 2010 Mentawai, Indonesia and 4 May 2018 Hawaii Island earthquakes. *Geophysical Research Letters*, *45*, 10,342-10,349. https://doi.org/10.1029/2018GL080042

Lin, G., & Okubo, P. G. (2020). Seismic evidence for a shallow detachment beneath Kilauea's south flank during the 2018 activity. *Geophysical Research Letters*, *47*, e2020GL088003. https://doi.org/10.1029/2020GL088003

Lipman, P. W., Lockwood, J. P., Okamura, R. T., Swanson, D. A., & Yamashita, K. M. (1985). *Ground deformation associated with the 1975 magnitude-7.2 earthquake and resulting changes in activity of Kilauea volcano, Hawaii*. (pp. 1–45). U.S. Geological Survey Professional Paper 1276.

Lipman, P. W., Normark, W. R., Moore, J. G., Wilson, J. B., & Gutmacher, C. E. (1988). The giant submarine Alika debris slide, Mauna Loa, Hawaii. *Journal of Geophysical Research*, *93*, 4279–4299. https://doi.org/10.1029/jb093ib05p04279

Liu, C., Lay, T., & Xiong, X. (2018). Rupture in the 4 May 2018 M_w 6.9 earthquake seaward of the Kilauea East Rift Zone fissure eruption in Hawaii. *Geophysical Research Letters*, *45*, 9508–9515. https://doi.org/10.1029/2018GL079349

Ma, K.-F., Kanamori, H., & Satake, K. (1999). Mechanism of the 1975 Kalapana, Hawaii, earthquake inferred from tsunami data. *Journal of Geophysical Research*, *104*, 13153–13167. https://doi.org/10.1029/1999jb900073

McMurtry, G. M., Fryer, G. J., Tappin, D. R., Wilkinson, I. P., Williams, M., Fietzke, J., et al. (2004). Megatsunami deposits on Kohala volcano, Hawaii, from flank collapse of Mauna Loa. *Geology*, *32*, 741–744. https://doi.org/10.1130/g20642.1

Montgomery-Brown, E. K., Segall, P., & Miklius, A. (2009). Kilauea slow slip events: Identification, source inversions, and relation to seismicity. *Journal of Geophysical Research*, *114*, B00A03. https://doi.org/10.1029/208JB006074

Moore, J. G., & Krivoy, H. L. (1964). The 1962 flank eruption of Kilauea volcano and structure of the east rift zone. *Journal of Geophysical Research*, *69*, 2033–2045. https://doi.org/10.1029/jz069i010p02033

Moore, J. G., Normark, W. R., & Holcomb, R. T. (1994). Giant Hawaiian landslides. *Annual Review of Earth and Planetary Sciences*, *22*, 119–144. https://doi.org/10.1146/annurev.ea.22.050194.001003

Morgan, J. K., Moore, G. F., & Clague, D. A. (2003). Slope failure and volcanic spreading along the submarine south flank of Kilauea volcano, Hawaii. *Journal of Geophysical Research*, *108*, 2415. https://doi.org/10.1029/2003JB002411

Morgan, J. K., Moore, G. F., Hills, D. J., & Leslie, S. (2000). Overthrusting and sediment accretion along Kilauea's mobile south flank, Hawaii: Evidence for volcanic spreading from marine seismic reflection data. *Geology*, *28*, 667–670. https://doi.org/10.1130/0091-7613(2000)028<0667:oasaak>2.3.co;2

Nakamura, K. (1980). Why do long rift zones develop in Hawaiian volcanos – A possible role o thick oceanic sediments. *Bulletin of the Volcanological Society of Japan*, *25*, 255–269.

Nettles, M., & Ekström, G. (2004). Long-period source characteristics of the 1975 Kalapana, Hawaii, earthquake. *Bulletin of the Seismological Society of America*, *94*, 422–429. https://doi.org/10.1785/0120030090

Okada, Y. (1985). Surface deformation due to shear and tensile faults in a half-space. *Bulletin of the Seismological Society of America*, *75*, 1125–1154. https://doi.org/10.1785/bssa0750041135

Owen, S., Segall, P., Freymueller, J., Miklius, A., Denlinger, R., Arnodottir, T., et al. (1985). Rapid deformation of the south flank of Kilauea Volcano, Hawaii. *Science*, *267*, 1328–1332.

Owen, S., Segall, P., Lisowski, M., Miklius, A., Denlinger, R., & Sako, M. (2000). Rapid deformation of Kilauea Volcano: Global Positioning System measurements between 1990 and 1996. *Journal of Geophysical Research*, *105*(B8), 18983–18998. https://doi.org/10.1029/2000jb900109

Owen, S. E., & Bürgmann, R. (2006). An increment of volcano collapse: Kinematics of the 1975 Kalpana, Hawaii, earthquake. *Journal of Volcanology and Geothermal Research*, *150*, 163–185. https://doi.org/10.1016/j.jvolgeores.2005.07.012

Park, J., Morgan, J. K., Zelt, C. A., Okubo, P. G., Peters, L., & Benesh, N. (2007). Comparative velocity structure of active Hawaiian volcanoes from 3-D onshore-offshore seismic tomography. *Earth and Planetary Science Letters*, *259*, 500–516. https://doi.org/10.1016/j.epsl.2007.05.008

Satake, K., Okada, M., & Abe, K. (1988). Tide gauge responses to tsunamis: Measurements at 40 tide gauge stations in Japan. *Journal of Marine Research*, *46*, 557–571. https://doi.org/10.1357/002224088785113504

Segall, P., Desmarais, E. K., Shelly, D., Miklius, A., & Cervelli, P. (2006). Earthquakes triggered by silent slip events on Kilauea volcano, Hawaii. *Nature*, *442*, 71–74. https://doi.org/10.1038/nature04938

Swanson, D. A., Duffield, W. A., & Fiske, R. S. (1976). Displacement of the south flank of Kilauea volcano: The result of forceful intrusion of magma into the rift zones. *Geological Survey Professional Paper*, *963*, 44. https://doi.org/10.3133/pp963

Tanioka, Y., & Satake, K. (1996). Tsunami generation by horizontal displacement of ocean bottom. *Geophysical Research Letters*, *23*(8), 861–864. https://doi.org/10.1029/96gl00736

Thurber, C. H., & Gripp, A. E. (1988). Flexure and seismicity beneath the south flank of Kilauea volcano and tectonic implications. *Journal of Geophysical Research*, *93*, 4271–4278. https://doi.org/10.1029/jb093ib05p04271

Tilling, R. I., Koyanagi, R. Y., Lipman, P. W., Rockwood, J. P., Moore, J. G., & Swanson, D. A. (1976). *Earthquakes and related Catastrophic events, Island of Hawaii, November 29, 1975: A preliminary report*. US Geological Survey Circular 740. https://doi.org/10.3133/cir740

Wood, H. O. (1914). On the earthquakes of 1868 in Hawaii. *Bulletin of the Seismological Society of America*, *4*, 169–203. https://doi.org/10.1785/bssa0040040169

Wyss, M. (1988). A proposed source model for the great Kau, Hawaii, earthquake of 1868. *Bulletin of the Seismological Society of America*, *78*(4), 1450–1462. https://doi.org/10.1785/bssa0780041450

Wyss, M., & Kovach, R. L. (1988). Comment on "A Single-Force Model for the 1975 Kalapana, Hawaii Earthquake" by Holly K. Eissler and Hiroo Kanamori. *Journal of Geophysical Research*, *93*, 8078–8082. https://doi.org/10.1029/jb093ib07p08078

Wyss, M., & Koyanagi, R. (1992a). *Isoseismal maps, macroseismic epicenters, and estimated magnitudes of historical earthquakes in the Hawaiian Islands*, US Geological Survey Bulletin 2006. https://doi.org/10.3133/b2006

Wyss, M., & Koyanagi, R. Y. (1992b). Seismic gaps in Hawaii. *Bulletin of the Seismological Society of America*, *82*, 1373–1387. https://doi.org/10.1785/bssa0820031373

Yamazaki, Y., Cheung, K. F., & Kowalik, Z. (2011). Depth-integrated, non-hydrostatic model with grid nesting for tsunami generation, propagation, and run-up. *International Journal for Numerical Methods in Fluids*, *67*(12), 2081–2107. https://doi.org/10.1002/fld.2485

Yamazaki, Y., Cheung, K. F., & Lay, T. (2018). A self-consistent fault-slip model for the 2011 Tohoku earthquake and tsunami. *Journal of Geophysical Research: Solid Earth*, *123*(2), 1425–1458. https://doi.org/10.1002/2017jb014749

Yamazaki, Y., Kowalik, Z., & Cheung, K. F. (2009). Depth-integrated, non-hydrostatic model for wave breaking and run-up. *International Journal for Numerical Methods in Fluids*, *61*(5), 473–497. https://doi.org/10.1002/fld.1952